Spinel of Nickel-Cobalt Oxide with Rod-Like Architecture as Electrocatalyst for Oxygen Evolution Reaction

Anna Dymerska, Wojciech Kukułka * , **Marcin Biegun** **and Ewa Mijowska**

Department of Nanomaterials Physicochemistry, West Pomeranian University of Technology, Piastow Av. 45, 70-311 Szczecin, Poland; anna.gabryela.dymerska@gmail.com (A.D.); marcin.biegun@zut.edu.pl (M.B.); ewa.borowiak-palen@zut.edu.pl (E.M.)

* Correspondence: wojciech_kukulka@zut.edu.pl

Abstract: The renewable energy technologies require electrocatalysts for reactions, such as the oxygen and/or hydrogen evolution reaction (OER/HER). They are complex electrochemical reactions that take place through the direct transfer of electrons. However, mostly they have high over-potentials and slow kinetics, that is why they require electrocatalysts to lower the over-potential of the reactions and enhance the reaction rate. The commercially used catalysts (e.g., ruthenium nanoparticles—Ru, iridium nanoparticles—Ir, and their oxides: RuO_2, IrO_2, platinum—Pt) contain metals that have poor stability, and are not economically worthwhile for widespread application. Here, we propose the spinel structure of nickel-cobalt oxide ($NiCo_2O_4$) fabricated to serve as electrocatalyst for OER. These structures were obtained by a facile two-step method: (1) One-pot solvothermal reaction and subsequently (2) pyrolysis or carbonization, respectively. This material exhibits novel rod-like morphology formed by tiny spheres. The presence of transition metal particles such as Co and Ni due to their conductivity and electron configurations provides a great number of active sites, which brings superior electrochemical performance in oxygen evolution and good stability in long-term tests. Therefore, it is believed that we propose interesting low-cost material that can act as a super stable catalyst in OER.

Keywords: spinel; electrocatalyst; oxygen evolution reaction; thermal treatment

1. Introduction

The fossil fuel combustion products have the most significant impact on air pollution [1], and with the increasing consumption of fossil fuel, it is of great importance for our planet to find some renewable energy resources to replace the traditional ones. These resources should deliver energy without a negative impact on the environment, and good examples could be wind, solar or hydrogen energy. Among green energy, hydrogen and oxygen are easily accessible energy carriers that can be a great answer to the sustained growth of energy requirements for the entire globe [2]. These crucial chemical reagents and fuels are produced via water splitting processes, such as hydrogen and oxygen evolution reactions (HER, and OER, respectively). These reactions are types of electrochemical reactions. Electrocatalysis is involved in electrochemical reactions at the interface of two phases: Electrode and electrolyte [3]. It is essential to mention that under typical operating conditions, only a few materials, used as an electrode, can achieve desirable stability [4]. That is the reason why the anodic, as well as a cathodic reactions, are generally catalyzed. The choice is mostly between noble metal and their oxides such as Pt, Ru, RuO_2, Ir, IrO_2. Furthermore, it is worth mentioning that Giordano et al. have recently reported Hf nanoparticles for OER, which exhibiting interesting performance and low over-potential [5].

Nowadays, many studies are focused on finding alternative electrocatalysts, mostly metal-based materials. It is due to their abilities to exhibit great catalytic activity. The main aim is to find an electrode material with better kinetics and stability during electrochemical reactions. Most studies are focused on nanomaterials containing Ru, Ir, and Rh nanoparticles [6], transition metal-based catalysts, e.g., transition-metal oxides (TMOs) [7], hydro(oxy)oxides [8], perovskites [9], spinels [10], metal monoxide structures, for instance, transition-metal dichalcogenides (TMDs) [11], nitrides (TMNs) [12] and phosphides (TMPs) [13], and non-metallic compounds [14]. Among TMOs with chemical formula AB_2O_4 and cubic crystallographic structure (especially $CoMn_2O_4$, $FeMn_2O_4$, $NiCo_2O_4$, $NiMn_2O_4$ and $ZnCo_2O_4$) have been claimed as promising anode materials for electrochemical use, e.g., LIBs, supercapacitors, and electrocatalysts mainly in OER [15]. These chemical compounds belong to the spinel group [16].

The name, "spinel", is used for all minerals with the cubic structure and general composition AB_2X_4, where A and B are metal cations (at the +1/+2/+4, and +2/+3 valences, respectively) and X is chalcogens anion (at the −1/−2/−3 valence, mostly oxygen). It is worth mentioning that the cations A and B can also be the same element, but with different valences, e.g., magnetite—Fe_3O_4 (with one atom of iron at 2+ and two atoms at +3 valences state) [17]. So far, 95 notable spinels have been reported [17]. Noteworthy, they have shown better properties in comparison with their simple counterpart—single metal TMOs. The explanation is the synergistic and complementary effect [18]. Their most popular applications are energy storage [19] (because of their variable chemical valances and redox capacitance), data storage [20] (they have demonstrated outstanding magnetism properties), optical devices like lasers [21] (due to electrochemical luminescence and photoluminescence), various reaction catalysis, e.g., HER [22], OER [23], oxygen reduction reaction (ORR) [24] (they have controllable composition, valence, structure, and morphology).

$NiCo_2O_4$ is an inverse spinel, which means the divalent cations swap place with half of the trivalent ones in its structure. In that case, the cations M^{2+} occupy octahedral sites [25]. Nickel-cobalt oxide has the $Fd3\overline{m}$ space group. In this compound, nickel is located on the octahedral sites (16d) and cobalt is in the octahedral and tetrahedral sites (16d, and 8a, respectively). It is claimed that the pairs of their redox cations (Ni^{3+}/Ni^{2+}, Co^{3+}/Co^{2+}) are distributed in the oxidation state of this spinel structure [26]. It has many advantages, such as good electrochemical performance (such as significant specific capacitance, high activity, splendid stability) and is noteworthy that it is environmentally friendly [27]. It is crucial to know that electrochemical properties strongly depend on its structure/shape. There are many reported methods of syntheses of $NiCo_2O_4$ particles that have found application in electrochemistry, for example, mesoporous nanoneedles with different shapes for electrochemical capacitor electrodes, that show outstanding capacitance of 932 Fg^{-1} (at 2.0 Ag^{-1}) and an imperceptibly small drop of specific capacitance after 3000 cycles (at 2.0 Ag^{-1}) [28]. The mesoporous flake-like nanoparticles $NiCo_2O_4$ for supercapacitor electrodes, with good electrochemical properties: 1125 Fg^{-1} (at 0.05 Ag^{-1}), coulombic efficiency after ~1600 cycles is 94% have been also reported [29]. Furthermore, the porous nanotubes composed of spinel as an electrochemical capacitor electrode with interesting capacitance 1647 Fg^{-1} (at 1.0 Ag^{-1}) and good capacity retention 77.3% (at 25.0 Ag^{-1}) show 6.4% capacitance loss after 3000 cycles [30].

This paper presents a simple synthesis of a $NiCo_2O_4$ spinel oxide via a one-pot solvothermal process. Nickel and cobalt precursors were picked for their high theoretical capacitance and similar potential during electrochemical reactions [31]. Our TMO particles have interesting architecture, representing spheres aggregated into rods. Keeping in mind the shape-dependent electrochemical performance of $NiCo_2O_4$ in OER, we provide a detailed characterization of rod-like materials thermally treated via pyrolysis, and carbonization, respectively. Scheme 1 presents a graphical representation of the structure used in the OER process.
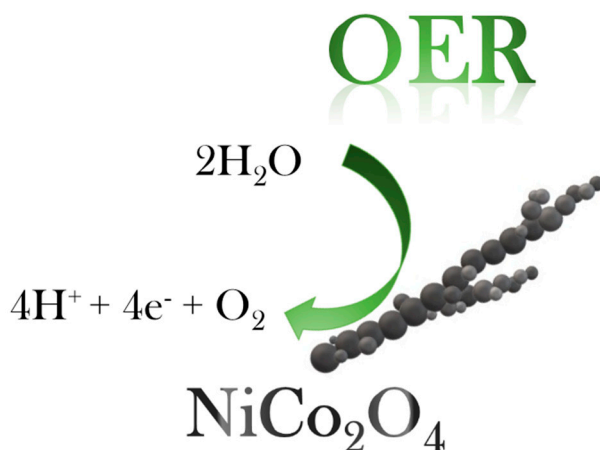
Scheme 1. The graphical representation of the structure used in OER process.

2. Materials and Methods

All reagents were used as received (in analytical grade). Ethylene glycol (EG) purchased from Chempur (Piekary Śląskie, Poland), was used as a solvent, nickel (II) acetate tetrahydrate ($Ni(OCOCH_3)_2 \cdot 4H_2O$, NA) and cobalt (II) acetate tetrahydrate ($Co(OCOCH_3)_2 \cdot 4H_2O$) both from Sigma Aldrich (Poznań, voivodeship: Wielkopolskie, Polska, Poland) were used as a metal precursor.

2.1. Synthesis of NiCo$_2$O$_4$

$Ni(OCOCH_3)_2 \cdot 4H_2O$ (257 mg) and $Co(OCOCH_3)_2 \cdot 4H_2O$ (498 mg) were dissolved in the 230 mL of EG via the ultrasonication. Next, the homogeneous solution was poured into a round-bottomed flask. Then, the solvothermal reaction was carried out under reflux at 180 °C for 12 h. After that, the product was washed with pure ethanol and decanted using an ultracentrifuge. The grey, tiny rod-like precipitate, which shown magnetic responses to the magnet, was dried at 60 °C for 12 h.

The second step was the thermal decomposition. As the product, $NiCo_2O_4$ was obtained after heating in a tube furnace. The calcination process was conducted for 4 h at 300 and 400 °C in the air (100 sccm). The obtained samples were marked as $NiCo_2O_4\_a300$, and $NiCo_2O_4\_a400$, respectively.

To investigate the effect of higher temperatures on the formation of a spinel structure, a carbonization process was also carried out for 4 h at 600 and 800 °C in an inert gas (100 sccm). The samples were named $NiCo_2O_4\_i600$, and $NiCo_2O_4\_i800$.

2.2. Characterization

The samples' morphology, geometry, and structure were analyzed with scanning electron microscopy (SEM, VEGA3 TESCAN, accelerating voltage at 100 kV, Tescan, Brno, Czech Republic). The characterization of chemical composition in the samples was investigated on the Raman spectroscopy (InViaRenishaw, Wotton-under-Edge, UK, laser 785 nm). The information about the crystallographic of the as-synthesized materials was provided by X-ray diffraction (XRD, AERIS PANalytical X-ray diffractometer with Cu-Kα radiation, Malvern, UK).

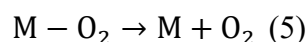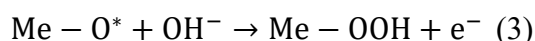### 2.3. Electrochemical Measurement/Reaction Mechanism

Electrochemical tests were made in a 3-electrode glass cell, by potentiostat station (BioLogic VMP-3, Seyssinet-Pariset, France), at the constant temperature of 25 ± 0.05 °C. The system was thermostated by a temperature control bath (Hubner KISS 6, Kassel, Germany). Short-time tests were carried out with an inert gas (Ar) electrolyte purging.

The working electrode (WE) potential was referred to the electrode made of mercury oxide (MOE) Hg|HgO, in alkaline electrolyte KOH (1 M solution). The measurements were calibrated to the Reversible Hydrogen Electrode (RHE) potential calculated by the following equation:

$E_{RHE} = E_{MOE} + 0.128 + 0.059 \cdot pH(V)$, where E_{RHE} is potential versus RHE and E_{MOE} is potential versus MOE. In order to obtain the value of the overpotential (η), the thermodynamic value of the oxygen reduction potential (i.e., 1.23 V) is subtracted from the experimental potential value. Platinum wire with the surface area of ~5 cm^2 served as the counter electrode (CE).

The working electrode (WE) was made of 10 mm × 10 mm with 125 μm thickness graphite foil (99.8%, GoodFellow, Hamburg, Germany). The active material was dispersed under ultra-sonification in a solution made of 20% of isopropanol/water with 0.05% of Nafion. The dispersion with final concentration 10 mg/mL was applied dropwise by volume 10 μL on each side on the surface of the WE and dried for 12 h at the 60 °C.

In general, during OER, there is a loss of electrons from water molecule (H_2O) or hydroxide ion (OH^-) and generating oxygen (O_2). The mechanism of this process on electrodes made of spinel particles is shown in the scheme below (see Scheme 2). The first step is the adsorption, followed by the discharge of the OH^- at the surface of a metal catalyst (Me) (1). The next step is the reaction of absorbed OH^- anions with the OH particles. The result is the production of H_2O and adsorption of atomic O* with simultaneous electron releasing (2). The next step is the reaction between O* atom and OH^- (3). The result is the formation of absorbed OOH particles. It is assumed that this is the step that limits the rate of the OER. Subsequently, the reaction with additional OH^- leads to form an adsorbed molecules of H_2O and O_2 (4). The final step is the desorption of the O_2 (5) [17]:

$$Me + OH^- \rightarrow Me - OH + e^- \quad (1)$$
$$Me - OH + OH^- \rightarrow Me - O^* + e^- + H_2O \quad (2)$$
$$Me - O^* + OH^- \rightarrow Me - OOH + e^- \quad (3)$$
$$Me - OOH + OH^- \rightarrow Me - O_2 + e^- + H_2O \quad (4)$$
$$M - O_2 \rightarrow M + O_2 \quad (5)$$

Scheme 2. The pathways of reactions during OER of spinels particles [17].

3. Results and Discussion

The architecture and morphology of the samples were observed via SEM. The obtained results are presented in Figure 1 and they clearly show that all the samples exhibit the rod-like structure which is made of tiny spheres with diameters of ~1.7 μm, ~4.3 μm, ~2.6 μm, ~3.0 μm, and ~1.8 μm, for precursor, pyrolyzed at 300 °C, 400 °C, carbonized at 600 °C, and 800 °C, respectively. The length of rods are ~52.2 μm, ~42.6 μm, ~ 50.9μm, ~90.0 μm, and ~51.3 μm, for precursor, pyrolyzed at 300 °C, 400 °C, carbonized at 600 °C, and 800 °C, respectively. The diameters of rods are estimated to be ~4.1 μm, ~5.8 μm, ~5.7 μm, ~4.5 μm, and ~1.9 μm, for precursor, pyrolyzed at 300 °C, 400 °C, carbonized at 600 °C, and 800 °C, respectively. Interestingly, the material retained the original shape of the particles after thermal treatment. The shape of the obtained spinels may result from the type of synthesis method used or the presence of additional templates. Devaguptapu et al. obtained typical $NiCo_2O_4$ spinel needle-like shapes and then modified them using various templates [32]. These needles consist of many nanoparticles with a size around 10–20 nm and have a greater tendency to aggregate in comparison to our material. Authors also proved that the electrochemical performance is high morphology-dependent. $NiCo_2O_4$ spinel can also take the form of nanowires. Jin et al. [33] synthesized tangled together nanowires composed of many nanoparticles. A similar morphology was repeated several more times. The urchin-like spheres composed by $NiCo_2O_4$ were obtained by Qin et al. [34]. In this case, samples have inverse geometry, where the spheres are made up of nanowires. Resembling morphology was reported by Chen et al. [35]. They obtained rambutan-like spinels microspheres. The same architecture has been reported by Li et al. [36]. The product has also shown the morphology of nanoneedles. This architecture was assembled radiantly into a rambutan-like structure. In our case, the structures are isolated, but are not as thin as wires and needles, and the rods are more like branches made of many spheres.
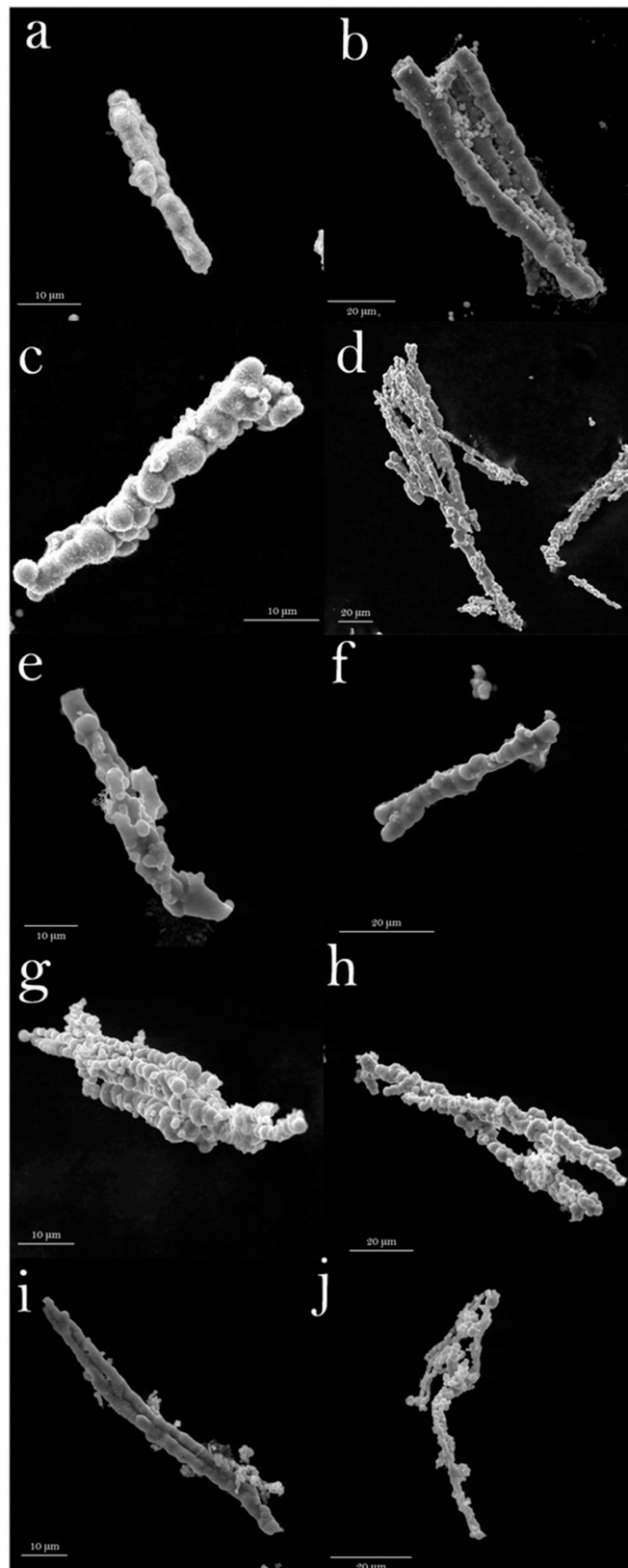
Figure 1. SEM images of samples: After solvothermal reaction (**a**,**b**), and after calcination: at 300 °C (**c**,**d**), and at 400 °C (**e**,**f**), after carbonization: at 600 °C (**g**,**h**) and at 800 °C (**i**,**j**).

The crystal structure of the metal oxide was analyzed using X-Ray Diffractometry (XRD) (Figure 2a). All reflections are well-indexed to $NiCo_2O_4$ cubic structure, confirmed by referencing with JCPDS card No. 20-0781. All diffractograms contain reflections at 2θ values of 20.14°, 30.59°, 36.11°, 41.96°, 43.54°, 50.82°, 58.72°, 61.42° and 75.48°. These values of degrees are corresponding to (111), (220), (311), (222), (400), (422), (511), (531), (440), and (533), respectively [37,38]. Furthermore, the XRD pattern shows reflections attributed to other species: Co_3O_4, and NiO. It has been referred with JCPDS card no. 43-1003, and 47-1049, respectively. These results clearly demonstrate Ni and Co's influence on the spinel structure and have been reported before [39,40]. The purity of samples was proved by the absence of any unidentified peak. The results confirm that 300 °C is high enough to obtain the crystalline $NiCo_2O_4$ spinel. Moreover, the calcinated samples have shown higher peaks than carbonized ones. This is due to the existence of a more significant number of oxygen vacancies. An increasing number of these vacancies is caused by the different partial pressure of the oxygen particles, which leads to a pronounced effect on the oxygen evolution [41].

The results obtained via Raman Spectroscopy are shown in Figure 2b. They present the vibronic properties and composition changes in the structure of the synthesized samples. The main peaks corresponding to the modes of spinel structure are in the range between 190 and 800 cm^{-1} and they are detected in each sample. A mode can be defined as an excitation state of a standing wave in a dynamical system. Specific one or few frequencies characterize each of them, so each store has a defined amount of energy. The modes are labelled by different letters (e.g., A, B, E, L), which assign vibrational movement to a particular group of points [42]. The highest intensity of peak is presented in samples calcinated at 300 °C. The height of the local maximum decreases with increasing temperature. The spectra show vibrational peaks precisely at 196, 482, 522, 621, and 692 cm^{-1}, which correspond to F_{2g}, E_g, F_{2g}, F_{2g}, and A_{1g} Co_3O_4 modes, respectively [43]. The A_{1g} mode is assigned to the vibrational moves of ions placed in octahedral sites, and the peaks at E_g and 522 cm^{-1} from F_{2g} mode are due to the occurring simultaneously vibrations of both octahedral and tetrahedral oxygen atoms in the crystal structure. Two Raman peaks present in the spectra at ~522 and 1100 cm^{-1} are assigned to NiO shaking peaks. The appearance of local maximum could be defined as the longitudinal optical (1LO) phonon modes of, and two-phonon (2P) 2LO modes of this compound [44]. The highest peaks in the pyrolyzed samples suggest that the air is the best thermal decomposition environment forming a well-crystallized structure: The higher peak, the stronger interaction between atoms Ni-Co-O [45]. Additionally, the Raman spectrum of the sample pyrolyzed at 300 °C exhibits only Co–O and Ni–O vibrational maximum, which proves the successful decomposition of both nickel and cobalt precursors, leading to form $NiCo_2O_4$. XRD data are in full agreement with Raman investigations.
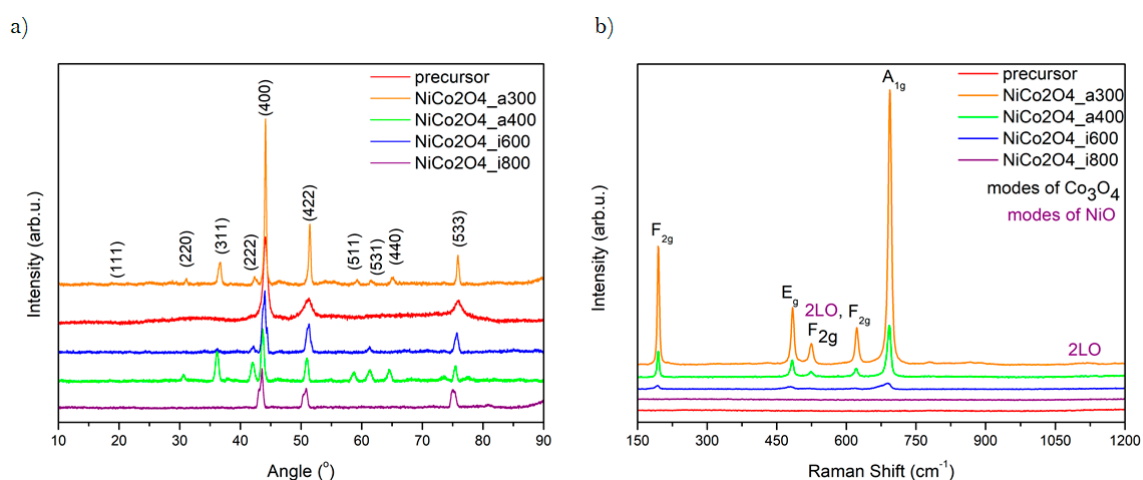

Figure 2. XRD patterns (**a**) and Raman Spectra (**b**) of obtained samples.

OER is a complementary reaction for HER, which proceeds simultaneously on CE. The prepared electrodes' electrocatalytic properties were tested in OER process, due to its higher energy barrier, which makes it rate-limiting process during water splitting. ORR is the reverse electrochemical reaction that takes place in fuel cells. The measurements were collected and performed by Linear Sweep Voltammetry (LSV). The main element of the system is a 3-electrode cell. As an electrolyte was used KOH (1 M concentration The sweep speed was at the level 5 mVs^{-1}, an IR drop factor made corrections. The surveys were carried out in order to achieve the absolute value of current density -25 mAcm^{-2} and potential below the standard potential during OER related to RHE (1.229 V vs. RHE). The data were collected to evaluate the samples' activity as the electrocatalysts, via its value of overpotential η [mV]. That value is a difference between thermodynamics in HER/OER at a specific current density. Mostly it is measured at 1 and 10 mAcm^{-2}, which is identified as η_1 and η_{10}, respectively. A better reaction rate is indicated by lower η value, which means the best catalytical activity has the lowest value of η.

The performances of the overpotential during LSV test in the OER process are included in and Figure 3a and Table 1. That the onset overpotentials of synthesized samples at a current density of 1 and 10 mAcm^{-2} are lower than or comparable to RuO$_2$, indicating great electrochemical activity. At a current density of 1 mAcm^{-2} the best performance exhibits the NiCo$_2$O$_4$_a400 (with η_1 326 mV). The NiCo$_2$O$_4$_a300 and NiCo$_2$O$_4$_a400 showed the best electrocatalytic performance at a current density of 10 mAcm^{-2} (both η_{10} 420 mV). However, it is essential to point out better results of all spinel samples than RuO$_2$, implying the critical role of high catalyst conductivity in the OER process.
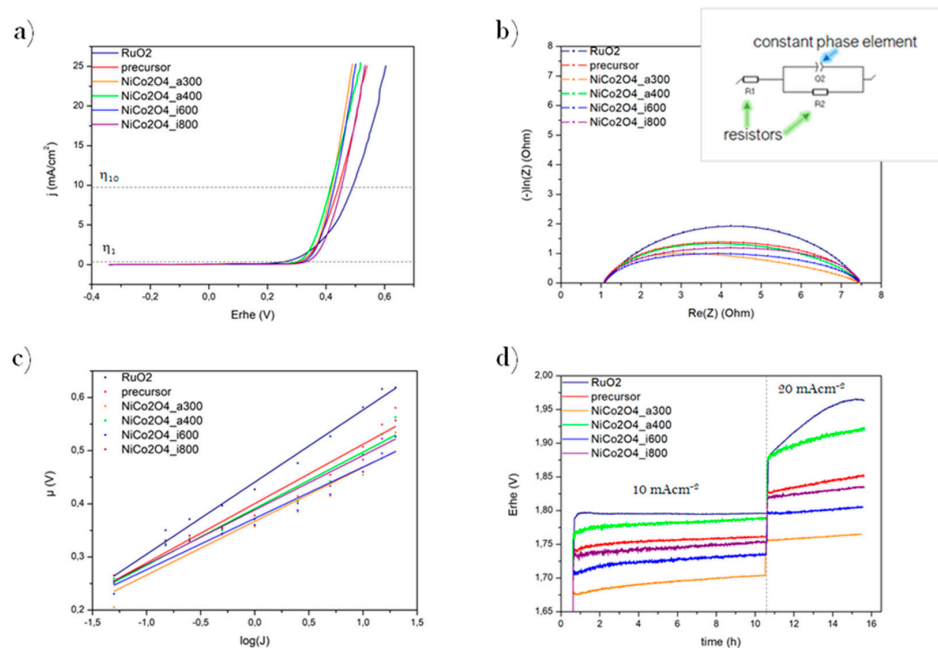

Figure 3. OER electrochemical measurements: LSV plots (**a**), Nyquist plots (with an inset graph window of equivalent Circuit R1R2Q) (**b**), Tafel plots (**c**), and chronopotentiometry plots (**d**) of the obtained materials compared to RuO$_2$.

The next measurement was carried out to collect accurate data about the electrochemical activity of catalysts via Galvanostatic Electrochemical Impedance Spectroscopy (GEIS). It was applied at current density 5 mAcm^{-2} with an amplitude of 10 mV at the frequency range between 100 mHz and 100 kHz. They were fitted on the BioLogic software to the equivalent circuit (R$_1$ + R$_2$)/Q via Z-fit electrochemical fitting program (Figure 3b). That circuit was chosen because it is the simplest one suitable for the measurement system. It contains, R1 which is the electrolyte resistance [Ω], which is linked in series with R$_2$—resistance of transfer an electric charge [Ω]. It is also connected in parallel with the element of constant phase Q (Fs$^{(a-1)}$)$^{-1}$. Real resistance R [Ω] is the abscissa value of the starting point at the diagram and it starts at the maximum of frequency. It represents the sum of the resistance of

all connectors and electrolyte. All these elements are linked together in series (marked as a R_1 resistor on the scheme). The diameter of the half-circle is calculated from points at X-axis. This parameter is the representation of the charge transfer resistance value (marked as R_2). Its vertical size is indicated as a Q element, representing a constant phase. The more developed the catalyst surface, the greater value of Q. The difference between diameters of semi-circles are results of a change in R_2 value, which is proportional to the inverse value of the intensity of the HER/OER process taking place on the electrode. In other words, lower R_2 value indicates the better activity of the electrocatalyst (under the same process conditions).

The differences in equivalent resistance during the OER process are implied in Figure 3b and Table 1. Presented Semi-circles have a similar shape and start in the same value in the abscissas axis. All samples have lower R_2 than RuO_2, which confirms the high activity of the synthesized materials. The lowest result indicates the best activity of 3.52 Ω is exhibited by $NiCo_2O_4$_a300, which suggests a better electrical conductivity and faster charge transport of the electrode.

For a better description of the electrochemical evolution process Tafel equation via steady-state chronopotentiometry (CP) have been revealed. For calculations was used a simple dependency: $f(x) = \eta = f(\log(j))$. The measurement of potentials on the WE occurs while maintaining different direct current (DC) for a certain time. Then the value of the Tafel slope is calculated using the linear regression method. The lower value of slope means a better catalyst activity, due to a faster electrochemical reaction rate.

The results of Tafel properties toward the OER process are shown and summarized in Figure 3c and Table 1. All the samples have lower slope values than RuO_2, indicating more effective electron transfer, and better catalytic activity during OER for $NiCo_2O_4$ spinel. The electrode composed of $NiCo_2O_4$_a300 has the most favorable electrocatalytic reaction kinetics, represented by the lowest value of the slope equal to 3.52 mVdec^{-1}.

Finally, for a complete description of the electrocatalytic activity, the stability tests have been conducted. The material used as electrocatalyst should exhibit high electroactivity and great durability in a long operation, which means that the minimum difference in overpotential is desirable. Chronopotentiometry method was used to examine the performance of samples. The measurement was performed in two stages: first stability was tested at a current density of 10 mAcm^{-2} for 10 h, followed by the second step at 20 mAcm^{-2} for the next 5 h. Relative changes in overpotentials over time was calculated with the following formula:

$$\left| \frac{f(x_1 - x_0)}{f(x_0)} \times 100\% \right| = \Delta\eta \tag{1}$$

where x_0 is the starting point of the plateau, and x_1 is the finishing point.

During the first step of a stability test (Figure 3d and Table 1), the overpotential exhibited by RuO_2 has the lowest relative growth (+0.56%), and among the obtained samples, the most stable turned out to be $NiCo_2O_4$_i800 (+0.57%). During the second step—at higher current density, the best stability performance, with constant overpotential, has been exhibited by $NiCo_2O_4$_i600. The stability chronopotentiometry long tests show that $NiCo_2O_4$ spinel particles are excellent candidates to use as OER catalyst material.

Table 1. Electrochemical properties of the obtained samples and RuO_2 during OER process: overpotential η_1 and η_{10}, Tafel slope, R_2 equivalent resistance values, and relative changes in overpotentials over time $\Delta\eta$.

Sample		η_1 [mV]	η_{10} [mV]	Tafel Slope [mV/dec]	R_2 [Ω]	$\Delta\eta_{10}$ [%]	$\Delta\eta_{20}$ [%]
RuO_2		312	491	136	6.40	0.56	4.26
Precursor		340	446	112	5.35	1.15	1.09
$NiCo_2O_4$	a300	346	420	101	3.52	1.19	0.57
	a400	328	420	106	4.85	1.13	2.13
	i600	346	430	97	3.89	1.75	0.00
	i800	359	454	103	4.95	0.57	0.55

The present state of the art report that the electrochemical performance of $NiCo_2O_4$ spinels in OER is shape-dependent. Table 2 presents the collected data on the main OER results measured with $NiCo_2O_4$ spinels with different architecture such as nanoflowers, nanospheres, nanoparticles, nanoflakes, and nanoflowers [46–52]. The main parameters are η at 10 $mAcm^{-2}$, Tafel slope and stability tests. However, not many contributions report the results on stability tests. Comparing them to our data shows that the proposed samples of spinels, with a rod-like structure composed by aggregated spheres, behave in a stable manner, even in the long-term. It can be further concluded that the synergy of spheres and rods provided efficient electrocatalysts with superior stability and promising activity. As mentioned before, Hf nanoparticles have been recently reported as a novel electrocatalyst with relatively low values of overpotential at 10 $mAcm^{-2}$ (358 mV) and Tafel slope of 85 mV/dec [5]. Therefore, it is desired to study these materials in greater detail and various morphology to reveal a clear correlation between spinels shape and their electrochemical performance.

Table 2. Comparison of morphologies and catalysts activity exhibited by $NiCo_2O_4$ spinel.

Architecture of the Sample	η [mV] (at 10 $mAcm^{-2}$)	Tafel Slope [mV/dec]	Persistence of Overpotential [%]	References
Rod-like	420	97	99 (10.5 h, 10 $mAcm^{-2}$) 100 (5 h, 20 $mAcm^{-2}$)	This work
Nanoflowers	383	137	47 (1 h, 6.8 $mVcm^{-2}$)	[46]
Hollow Nanospheres	428	141	31 (1 h, 3.5 $mVcm^{-2}$)	
	520	150	96 (12 h, 1.76 V)	[47]
Urchin Nanospheres	441 (at 5 $mAcm^{-2}$)	103	91 (12 h, 1.76 V)	
Nanoparticles	422	136	-	[48]
	500	119	-	[49]
Nanoflakes	430	76	87 (24 h, 10 $mAcm^{-2}$)	[50]
	360	131	-	[51]
Nanowires	271	172	-	[52]

4. Conclusions

In conclusion, $NiCo_2O_4$ rod-like catalysts were successfully fabricated in a two-step process: Solvothermal reaction and annealing route as a facile route to synthesize spinel particles. The results collected from X-ray diffractogram and Raman spectroscope affirmed the formation of nickel-cobalt oxide compounds. These samples, with novel morphology, exhibited outstanding catalytic activity in the oxygen evolution reactions. Fabricated spinel material showed excellent electrochemical properties for the OER, better than commercial RuO_2: It is due to the presence of a high quantity of metals nanoparticles. A different condition during thermal treatment has been investigated to compare the influence of temperature, as well as the gas atmosphere on electrocatalytic activity. All samples were tested in a variety of electrochemical measurements during the OER process. As all summarized results have shown, the best electrochemical performance is exhibited by $NiCo_2O_4\_a300$ sample, which has high activity (due to low overpotential $\eta_1 = 346$, $\eta_{10} = 420$ mV, low Tafel slope = 101 mV/dec, and equivalent resistance $R_2 = 3.52\ \Omega$) as catalysts and almost constant overpotential during a long-term test (high persistence at level ~98.81% during I step, and ~99.43% during II step), which demonstrate the crucial roles of oxygen vacancies, which are created with larger amount during annealing under air atmosphere.

Author Contributions: Conceptualization, W.K. and E.M.; methodology, W.K. and M.B.; formal analysis, A.D., W.K. and M.B.; investigation, A.D. and W.K.; writing—original draft preparation, A.D. and W.K.; writing—review and editing, E.M.; visualization, A.D., W.K. and M.B.; supervision, E.M. All authors have read and agreed to the published version of the manuscript.

References

1. Zhang, S. Air Pollution Is Killing More People Than Smoking—And Fossil Fuels Are Large to Blame. Pacific Standard. Available online: https://psmag.com/environment/air-pollution-is-killing-more-people-than-smoking-and-fossil-fuels-are-largely-to-blame (accessed on 5 February 2020).
2. Xu, X.; Zhong, W.; Zhang, L.; Liu, G.; Du, Y. MoS2/NiS heterostructure grown on Nickel Foam as highly efficient bifunctional electrocatalyst for overall water splitting. *Int. J. Hydrogen Energy* **2020**, *45*, 17329–17338. [CrossRef]
3. Groß, A. Computational modeling of electrocatalytic reactions. In *Encyclopedia of Interfacial Chemistry*; Elsevier: New York, NY, USA, 2018; pp. 455–465, ISBN 978-0-12-809894-3.
4. Yuan, N.; Jiang, Q.; Li, J.; Tang, J. A review on non-noble metal based electrocatalysis for the oxygen evolution reaction. *Arab. J. Chem.* **2020**, *13*, 4294–4309. [CrossRef]
5. Defilippi, C.; Shinde, D.V.; Dang, Z.; Manna, L.; Hardacre, C.; Greer, A.J.; D'Agostino, C.; Giordano, C. HfN nanoparticles: An unexplored catalyst for the electrocatalytic oxygen evolution reaction. *Angew. Chem. Int. Ed.* **2019**, *58*, 15464–15470. [CrossRef]
6. Chaturvedi, S.; Dave, P.N.; Shah, N.K. Applications of nano-catalyst in new era. *J. Saudi Chem. Soc.* **2012**, *16*, 307–325. [CrossRef]
7. Elayappan, V.; Shanmugam, R.; Chinnusamy, S.; Yoo, D.J.; Mayakrishnan, G.; Kim, K.; Noh, H.S.; Kim, M.K.; Lee, H. Three-dimensional bimetal TMO supported carbon based electrocatalyst developed via dry synthesis for hydrogen and oxygen evolution. *Appl. Surf. Sci.* **2020**, *505*, 144642. [CrossRef]
8. Kandiel, T.A. Iron-incorporated NiS/Ni(OH)2 composite as an efficient electrocatalyst for hydrogen evolution reaction from water in a neutral medium. *Appl. Catal. A Gen.* **2019**, *586*, 117226. [CrossRef]
9. Feng, W.; Chen, H.; Zhang, Q.; Gao, R.; Zou, X. Lanthanide-regulated oxygen evolution activity of face-sharing IrO6 dimers in 6H-perovskite electrocatalysts. *Chin. J. Catal.* **2020**, *41*, 1692–1697. [CrossRef]
10. Liu, X.-M.; Cui, X.; Dastafkan, K.; Wang, H.-F.; Tang, C.; Zhao, C.; Chen, A.; He, C.; Han, M.; Zhang, Q. Recent advances in spinel-type electrocatalysts for bifunctional oxygen reduction and oxygen evolution reactions. *J. Energy Chem.* **2020**, *53*, 290–302. [CrossRef]
11. Hwang, J.; Noh, S.H.; Han, B. Design of active bifunctional electrocatalysts using single atom doped transition metal dichalcogenides. *Appl. Surf. Sci.* **2019**, *471*, 545–552. [CrossRef]
12. Theerthagiri, J.; Lee, S.J.; Murthy, A.P.; Madhavan, J.; Choi, M.Y. Fundamental aspects and recent advances in transition metal nitrides as electrocatalysts for hydrogen evolution reaction: A review. *Curr. Opin. Solid State Mater. Sci.* **2020**, *24*, 100805. [CrossRef]
13. Men, Y.; Li, P.; Zhou, J.; Chen, S.; Luo, W. Trends in alkaline hydrogen evolution activity on cobalt phosphide electrocatalysts doped with transition metals. *Cell Rep. Phys. Sci.* **2020**, 100136. [CrossRef]
14. Liang, X.; Wu, C.-M.L. Metal-free two-dimensional phosphorus carbide as an efficient electrocatalyst for hydrogen evolution reaction comparable to platinum. *Nano Energy* **2020**, *71*, 104603. [CrossRef]
15. Kong, X.; Zhu, T.; Cheng, F.; Zhu, M.; Cao, X.; Liang, S.; Cao, G.; Pan, A. Uniform MnCo2O4 porous dumbbells for lithium-ion batteries and oxygen evolution reactions. *ACS Appl. Mater. Interfaces* **2018**, *10*, 8730–8738. [CrossRef] [PubMed]
16. Bragg, W.H. The structure of magnetite and the spinels. *Nature* **1915**, *95*, 561. [CrossRef]
17. Zhao, Q.; Yan, Z.; Chen, C.; Chen, J. Spinels: Controlled preparation, oxygen reduction/evolution reaction application, and beyond. *Chem. Rev.* **2017**, *117*, 10121–10211. [CrossRef]
18. Huang, G.; Guo, X.; Cao, X.; Tian, Q.; Sun, H. Formation of graphene-like 2D spinel $MnCo_2O_4$ and its lithium storage properties. *J. Alloys Compd.* **2017**, *695*, 2937–2944. [CrossRef]
19. Park, M.-S.; Kim, J.; Kim, K.J.; Lee, J.-W.; Kim, J.H.; Yamauchi, Y. Porous nanoarchitectures of spinel-type transition metal oxides for electrochemical energy storage systems. *Phys. Chem. Chem. Phys.* **2015**, *17*, 30963–30977. [CrossRef]
20. Tatarchuk, T.; Bououdina, M.; Judith Vijaya, J.; John Kennedy, L. Spinel ferrite nanoparticles: Synthesis, crystal structure, properties, and perspective applications. In *Nanophysics, Nanomaterials, Interface Studies, and Applications*; Fesenko, O., Yatsenko, L., Eds.; Springer Proceedings in Physics; Springer International Publishing: Cham, Switzerland, 2017; Volume 195, pp. 305–325, ISBN 978-3-319-56244-5.
21. Jouini, A.; Yoshikawa, A.; Brenier, A.; Fukuda, T.; Boulon, G. Optical properties of transition metal ion-doped MgAl2O4 spinel for laser application. *Phys. Stat. Sol.* **2007**, *4*, 1380–1383. [CrossRef]

22. Walter, M.G.; Warren, E.L.; McKone, J.R.; Boettcher, S.W.; Mi, Q.; Santori, E.A.; Lewis, N.S. Solar Water Splitting Cells. *Chem. Rev.* **2010**, *110*, 6446–6473. [CrossRef]

23. Cheng, F.; Shen, J.; Peng, B.; Pan, Y.; Tao, Z.; Chen, J. Rapid room-temperature synthesis of nanocrystalline spinels as oxygen reduction and evolution electrocatalysts. *Nat. Chem.* **2011**, *3*, 79–84. [CrossRef]

24. Liang, Y.; Wang, H.; Zhou, J.; Li, Y.; Wang, J.; Regier, T.; Dai, H. Covalent hybrid of spinel manganese–cobalt oxide and graphene as advanced oxygen reduction electrocatalysts. *J. Am. Chem. Soc.* **2012**, *134*, 3517–3523. [CrossRef] [PubMed]

25. Bhattacharya, J.; Wolverton, C. Relative stability of normal vs. inverse spinel for 3d transition metal oxides as lithium intercalation cathodes. *Phys. Chem. Chem. Phys.* **2013**, *15*, 6486–6498. [CrossRef] [PubMed]

26. Li, Y.; Hasin, P.; Wu, Y. NixCo3−xO4 nanowire arrays for electrocatalytic oxygen evolution. *Adv. Mater.* **2010**, *22*, 1926–1929. [CrossRef] [PubMed]

27. Jiang, H.; Ma, J.; Li, C. Hierarchical porous NiCo2O4 nanowires for high-rate supercapacitors. *Chem. Commun.* **2012**, *48*, 4465–4467. [CrossRef] [PubMed]

28. Zhang, D.; Yan, H.; Lu, Y.; Qiu, K.; Wang, C.; Zhang, Y.; Liu, X.; Luo, J.; Luo, Y. NiCo2O4 nanostructure materials: Morphology control and electrochemical energy storage. *Dalton Trans.* **2014**, *43*, 15887–15897. [CrossRef]

29. Bhojane, P.; Sen, S.; Shirage, P.M. Enhanced electrochemical performance of mesoporous $NiCo_2O_4$ as an excellent supercapacitive alternative energy storage material. *Appl. Surf. Sci.* **2016**, *377*, 376–384. [CrossRef]

30. Li, L.; Peng, S.; Cheah, Y.; Teh, P.; Wang, J.; Wee, G.; Ko, Y.; Wong, C.; Srinivasan, M. Electrospun porous $NiCo_2O_4$ nanotubes as advanced electrodes for electrochemical capacitors. *Chem. Eur. J.* **2013**, *19*, 5892–5898. [CrossRef]

31. Uke, S.J.; Akhare, V.P.; Meshram-Mardikar, S.P.; Bodade, A.B.; Chaudhari, G.N. PEG assisted hydrothermal fabrication of undoped and Cr doped $NiCo_2O_4$ nanorods and their electrochemical performance for supercapacitor application. *Adv. Sci. Eng. Med.* **2019**, *11*, 357–366. [CrossRef]

32. Devaguptapu, S.V.; Hwang, S.; Karakalos, S.; Zhao, S.; Gupta, S.; Su, D.; Xu, H.; Wu, G. Morphology control of carbon-free spinel NiCo2O4 catalysts for enhanced bifunctional oxygen reduction and evolution in alkaline media. *ACS Appl. Mater. Interfaces* **2017**, *9*, 44567–44578. [CrossRef]

33. Jin, C.; Lu, F.; Cao, X.; Yang, Z.; Yang, R. Facile synthesis and excellent electrochemical properties of $NiCo_2O_4$ spinel nanowire arrays as a bifunctional catalyst for the oxygen reduction and evolution reaction. *J. Mater. Chem. A* **2013**, *1*, 12170–12177. [CrossRef]

34. Qin, Z.; Cheng, Q.; Lu, Y.; Li, J. Facile synthesis of hierarchically mesoporous $NiCo_2O_4$ nanowires for sensitive nonenzymatic glucose detection. *Appl. Phys. A* **2017**, *123*, 492. [CrossRef]

35. Chen, H.; Jiang, G.; Yu, W.; Liu, D.; Liu, Y.; Li, L.; Huang, Q. Electrospun carbon nanofiberic coated with ambutan-like $NiCo_2O_4$ microspheres as electrode materials. *MRC* **2017**, *7*, 90–96. [CrossRef]

36. Li, C.; Ge, Y.; Jiang, X.; Zhang, Z.; Yu, L. The rambutan-like C@$NiCo_2O_4$ composites for enhanced microwave absorption performance. *J. Mater. Sci. Mater. Electron.* **2019**, *30*, 3124–3136. [CrossRef]

37. Khalid, S.; Cao, C.; Wang, L.; Zhu, Y. Microwave assisted synthesis of porous $NiCo_2O_4$ microspheres: Application as high performance asymmetric and symmetric supercapacitors with large areal capacitance. *Sci. Rep.* **2016**, *6*, 22699. [CrossRef]

38. Li, T.; Li, X.; Wang, Z.; Guo, H.; Li, Y. A novel NiCo2O4 anode morphology for lithium-ion batteries. *J. Mater. Chem. A* **2015**, *3*, 11970–11975. [CrossRef]

39. Yan, H.; Zhang, D.; Xu, J.; Lu, Y.; Liu, Y.; Qiu, K.; Zhang, Y.; Luo, Y. Solution growth of NiO nanosheets supported on Ni foam as high-performance electrodes for supercapacitors. *Nanoscale Res. Lett.* **2014**, *9*, 424. [CrossRef] [PubMed]

40. Béjar, J.; Álvarez-Contreras, L.; Ledesma-García, J.; Arjona, N.; Arriaga, L.G. Electrocatalytic evaluation of Co_3O_4 and $NiCo_2O_4$ rosettes-like hierarchical spinel as bifunctional materials for oxygen evolution (OER) and reduction (ORR) reactions in alkaline media. *J. Electroanal. Chem.* **2019**, *847*, 113190. [CrossRef]

41. Wei, B.; Wu, J.; Mei, G.; Qi, Z.; Hu, W.; Wang, Z. NiCo2O4 nanowire arrays rich in oxygen deficiencies for hydrogen evolution reaction. *Int. J. Hydrogen Energy* **2019**, *44*, 6612–6617. [CrossRef]

42. Larbi, T.; Doll, K.; Amlouk, M. Temperature dependence of Raman spectra and first principles study of $NiMn_2O_4$ magnetic spinel oxide thin films. Application in efficient photocatalytic removal of RhB and MB dyes. *Spectrochim. Acta Part A Mol. Biomol. Spectrosc.* **2019**, *216*, 117–124. [CrossRef]

43. Umeshbabu, E.; Rajeshkhanna, G.; Justin, P.; Rao, G.R. Magnetic, optical and electrocatalytic properties of urchin and sheaf-like $NiCo_2O_4$ nanostructures. *Mater. Chem. Phys.* **2015**, *165*, 235–244. [CrossRef]

44. Mironova-Ulmane, N.; Kuzmin, A.; Sildos, I.; Pärs, M. Polarisation dependent Raman study of single-crystal nickel oxide. *Open Phys.* **2011**, *9*, 1096–1099. [CrossRef]

45. Huang, Y.; Fan, W.; Long, B.; Li, H.; Qiu, W.; Zhao, F.; Tong, Y.; Ji, H. Alkali-modified non-precious metal 3D-$NiCo_2O_4$ nanosheets for efficient formaldehyde oxidation at low temperature. *J. Mater. Chem. A* **2016**, *4*, 3648–3654. [CrossRef]

46. Li, Z.; Li, B.; Chen, J.; Pang, Q.; Shen, P. Spinel $NiCo_2O_4$ 3-D nanoflowers supported on graphene nanosheets as efficient electrocatalyst for oxygen evolution reaction. *Int. J. Hydrogen Energy* **2019**, *44*, 16120–16131. [CrossRef]

47. Wang, J.; Fu, Y.; Xu, Y.; Wu, J.; Tian, J.-H.; Yang, R. Hierarchical $NiCo_2O_4$ hollow nanospheres as high efficient bi-functional catalysts for oxygen reduction and evolution reactions. *Int. J. Hydrogen Energy* **2016**, *41*, 8847–8854. [CrossRef]

48. Lv, X.; Zhu, Y.; Jiang, H.; Yang, X.; Liu, Y.; Su, Y.; Huang, J.; Yao, Y.; Li, C. Hollow mesoporous $NiCo_2O_4$ nanocages as efficient electrocatalysts for oxygen evolution reaction. *Dalton Trans.* **2015**, *44*, 4148–4154. [CrossRef] [PubMed]

49. Yan, K.-L.; Shang, X.; Gao, W.-K.; Dong, B.; Li, X.; Chi, J.-Q.; Liu, Y.-R.; Chai, Y.-M.; Liu, C.-G. Ternary $MnO_2/NiCo_2O_4$/NF with hierarchical structure and synergistic interaction as efficient electrocatalysts for oxygen evolution reaction. *J. Alloys Compd.* **2017**, *719*, 314–321. [CrossRef]

50. Ganguli, S.; Das, S.; Kumari, S.; Inta, H.R.; Tiwari, A.K.; Mahalingam, V. Effect of intrinsic properties of anions on the electrocatalytic activity of $NiCo_2O_4$ and $NiCo_2O_xS_4$-x grown by chemical bath deposition. *ACS Omega* **2018**, *3*, 9066–9074. [CrossRef] [PubMed]

51. Yin, X.; Sun, G.; Wang, L.; Bai, L.; Su, L.; Wang, Y.; Du, Q.; Shao, G. 3D hierarchical network $NiCo_2S_4$ nanoflakes grown on Ni foam as efficient bifunctional electrocatalysts for both hydrogen and oxygen evolution reaction in alkaline solution. *Int. J. Hydrogen Energy* **2017**, *42*, 25267–25276. [CrossRef]

52. Gong, Y.; Pan, H.; Xu, Z.; Yang, Z.; Lin, Y.; Zhang, M. A Co_2O_4 (A=Ni, Zn, Mn) nanostructure arrays grown on nickel foam as efficient electrocatalysts for oxygen evolution reaction. *Int. J. Hydrogen Energy* **2018**, *43*, 14360–14368. [CrossRef]